Enhanced photocatalytic degradation of 2-chlorophenol over Z-scheme heterojunction of CdS-decorated oxygen-doped g-C$_3$N$_4$ under visible-light

Zhuzhu Zhang [a], Rui Ji [a], Qimeng Sun [a], Jinghui He [a], Dongyun Chen [a], Najun Li [a], Hua Li [a], Antonio Marcomini [b], Qingfeng Xu [a,*], Jianmei Lu [a,*]

[a] College of Chemistry, Chemical Engineering and Materials Science, Collaborative Innovation Center of Suzhou Nano Science and Technology, Soochow University, Suzhou, Jiangsu 215123, China
[b] Department of Environmental Sciences, Informatics and Statistics, University Ca' Foscari Venice, I-30170 Venice, Italy

ARTICLE INFO

ABSTRACT

Constructing photocatalysts with outstanding visible light utilization efficiency and a high-efficiency photo-generated charge transfer rate is the key to the photodegradation of organic pollutants in wastewater. Oxygen-doped graphitic carbon nitride (g-C$_3$N$_4$) responsive to a broad visible light range was prepared, to which CdS nanoparticles (NPs) were anchored to fabricate a Z-scheme heterojunction, constructing abundant charge transport orbitals that facilitate interfacial photo-generated charge separation. Meanwhile, density functional theory (DFT) calculations and electron spin resonance (ESR) tests proved that oxygen-doped g-C$_3$N$_4$/CdS-3 (O-CN/CdS-3) followed the Z-scheme charge transfer mechanism. The results showed that O-CN/CdS-3 degraded 10 ppm of 2-chlorophenol (2-CP) within 60 min, with a degradation rate constant (k = 0.10832) of around 11.5-fold that of g-C$_3$N$_4$ (0.00945). Furthermore, the active species and main intermediate products were also studied to explore the possible degradation pathway of 2-CP. Overall, this strategy provides insight for constructing other Z-scheme heterojunction photocatalysts for the efficient degradation of CPs.

1. Introduction

Chlorophenols (CPs) are refractory and highly toxic organic pollutants widely existing in wastewater, where they posed a serious threat to human health, even at a low concentration [1,2]. As a result, CPs are included in the list of pollutants under priority control by many countries. Chlorophenols have strong biotoxicity and antidegradation stability [3]. Many conventional approaches were used to degrade chlorophenols such as physicochemical, and biochemical techniques [4]. However, the p–π conjugation between chlorine (Cl) and the phenyl ring means that the C–Cl bonds in CPs are difficult to break, with chlorine band by-products as secondary pollutants in the environment [5]. Semiconductor photocatalytic had been extensively used in the degradation of organic pollutants owing to its economic and environmentally friendly, which can degrade organic pollutants into CO$_2$ and H$_2$O at room temperature [6]. However, there are still some defects, such as poor light absorption ability and low photo-generated charges transfer rate, which limited their further application [7,8]. These problems can be overcome by constructing heterojunction to broaden the light response range and promote photo-generated charge transfer.

Graphitic carbon nitride (g-C$_3$N$_4$) is the most extensively reported metal-free polymer photocatalyst with a large conjugated π structure, which has attracted wide attention due to its stable chemical properties, and simply preparation [8,9]. While the photocatalytic activity of g-C$_3$N$_4$ is limited owing to the ready recombination of its photo-generated charges, large sample size, and low specific surface area [10]. To address this, many novel synthesis techniques and modification methods were probed to polish up the photocatalytic activity of g-C$_3$N$_4$, among which elemental doping had been proved to be a particularly effective method. Recently, based on nonmetal heteroatom (oxygen (O)[11], sulfur (S) [12], and phosphorus (P) [13]) doping was an efficient strategy by which to tailor the bandgap and improve the migration efficiency of the photo-generated charges of photocatalysts, O-doping has attracted much attention due to its simple execution and the good photocatalytic performance. Wang et al. [14] synthesized O-doped g-C$_3$N$_4$ by adding different amounts of formic acid to adjust its bandgap, improve its light absorption ability, and promote charge transfer. Jiang et al. [15] prepared a porous O-doped g-C$_3$N$_4$ with

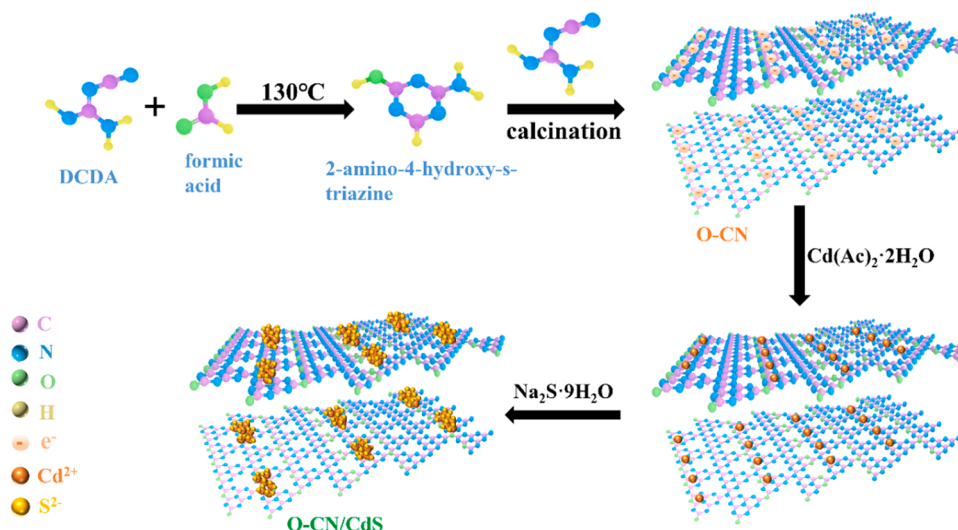**Scheme 1.** The synthetic procedure of Z-scheme O-CN/CdS heterostructure.

nitrogen defects via a one-pot co-pyrolysis method, where the O-doping increased BET (Brunauer–Emmett–Teller) surface area of the porous structure of g-C$_3$N$_4$ and polished up its light absorption ability. Above all, the O-doping of g-C$_3$N$_4$ can be used to increase the surface area and adjust the bandgap of g-C$_3$N$_4$ to achieve band matching with other semiconductors. Therefore, based on these advantages of the O-doping of g-C$_3$N$_4$, it is necessary to combine O-doped g-C$_3$N$_4$ with other semiconductors to improve its photocatalytic performance.

Z-scheme heterojunction has a suitable band structure, efficient charge transfer rate, and excellent redox performance, which contribute to the synthesis of a material that exhibits excellent photocatalytic activity [16]. Cadmium sulfide (CdS) is a material that has an easily adjustable band structure and a high charge separation rate [17]. Moreover, the morphology of CdS played a great role in its photocatalytic performance, with morphologies such as hollow nanostructures [18], nanorods [19], nanowires [20], and nanospheres [21] having been reported. CdS with a small particle size exhibit a relatively high surface area, leading to an obvious improvement in the migration rate of its electron-hole pairs [22], making it a good choice for constructing a heterojunction with g-C$_3$N$_4$. A series of g-C$_3$N$_4$/CdS conventional type II heterojunctions were reported in the literature [23]. Among these conventional type II g-C$_3$N$_4$/CdS heterojunctions, it was difficult to ensure the formation of a compact heterojunction interface and control the direction of electron-hole transport between interfaces to obtain the best photocatalytic performance using these methods. Moreover, CdS is prone to be oxidized into S and Cd^{2+} by its own photo-generated holes [24], thus, it is very significant to construct a novel heterojunction that meets the requirement that the photo-generated holes do not stay in the valence band (VB) of CdS.

In this work, O-CN/CdS-3 heterojunction was synthesized by anchoring CdS NPs onto the O-doped g-C$_3$N$_4$. The introduction of O adjusted the band structure of g-C$_3$N$_4$ to broaden the light response range. The formation of Z-scheme heterojunction promoted interfacial photo-generated charge separation. Benefiting from the above, O-CN/CdS-3 obtained the max photodegradation rate, showing the degradation of 2-CP (10 ppm) within 60 min under visible light. The Z-type heterojunction was then further investigated by density functional theory (DFT) calculations and electron spin resonance (ESR) measurements to clarify the interfacial charge transfer pathway. Additionally, the effects of different external factors such as catalyst dosage, 2-CP concentration, pH, anion, and water sources on the photodegradation of 2-CP. In general, the synergistic effect of Z-type O-CN/CdS heterojunction promoted charge separation and enhanced the photodegradation activity of chlorophenol under visible light, which obtained universal

applicability and long-term stability. Finally, we proposed the transfer pathway of photo-generated carriers, and explored the possible degradation pathway of 2-CP.

2. Experimental section

2.1. Materials

All materials employed in this study are listed in the Supplementary Material section.

2.2. Sample preparation

2.2.1. Preparation of oxygen-doped g-C$_3$N$_4$ (denoted as O-CN)
O-CN was synthesized according to previous literature reports [14] (See Supplementary Material for details).

2.2.2. Preparation of O-CN/CdS
O-CN/CdS photocatalyst was prepared by the in-situ solvothermal method. Firstly, put 0.1 g of O-CN into 80 mL of deionized water and sonicated for 30 min, then added 3 mg of Cd(Ac)$_2$·2 H$_2$O into the above solution and violently stirred for 1 h. Finally, put 2.6 mg of Na$_2$S·9 H$_2$O and violently stirred for 15 min. Then transferred the mixture into a 100 mL autoclave and reacted at 160 ℃ for 12 h. The product was washed with deionized water and ethanol three times and finally dried at 55 ℃ for 12 h. The resulting product was named O-CN/CdS-1. The collected products with different CdS vs O-CN mass ratios of 3%, 5%, 7%, and 9% were named CdS/O-CN-x (x = 1,2,3,4).

2.3. Photocatalytic measurements

To investigate the photocatalytic activity of the samples, 2-chlorophenol (2-CP), 4-chlorophenol (4-CP), and 2,4-dichlorophenol (2,4-DCP) were degraded under a 300 W xenon lamp (filter cut-off wavelength of 420 nm) irradiation. The reaction apparatus was shown in Fig. S1. Typically, put 21 mg of the synthesized samples into 30 mL of 10 ppm 2-CP reaction solution without pH value adjustment, and the mixture stir for 30 min under the dark. Upon reaching the adsorption equilibrium, turn on the light, and take samples every 20 min. To determine the concentration of 2-CP by using a high-performance liquid chromatography (HPLC) system. The intermediate products of 2-CP in the degradation process were detected by a liquid chromatography connected to a mass spectrometer (LC-MS). The removal rate of the pollutant was calculated as follow:
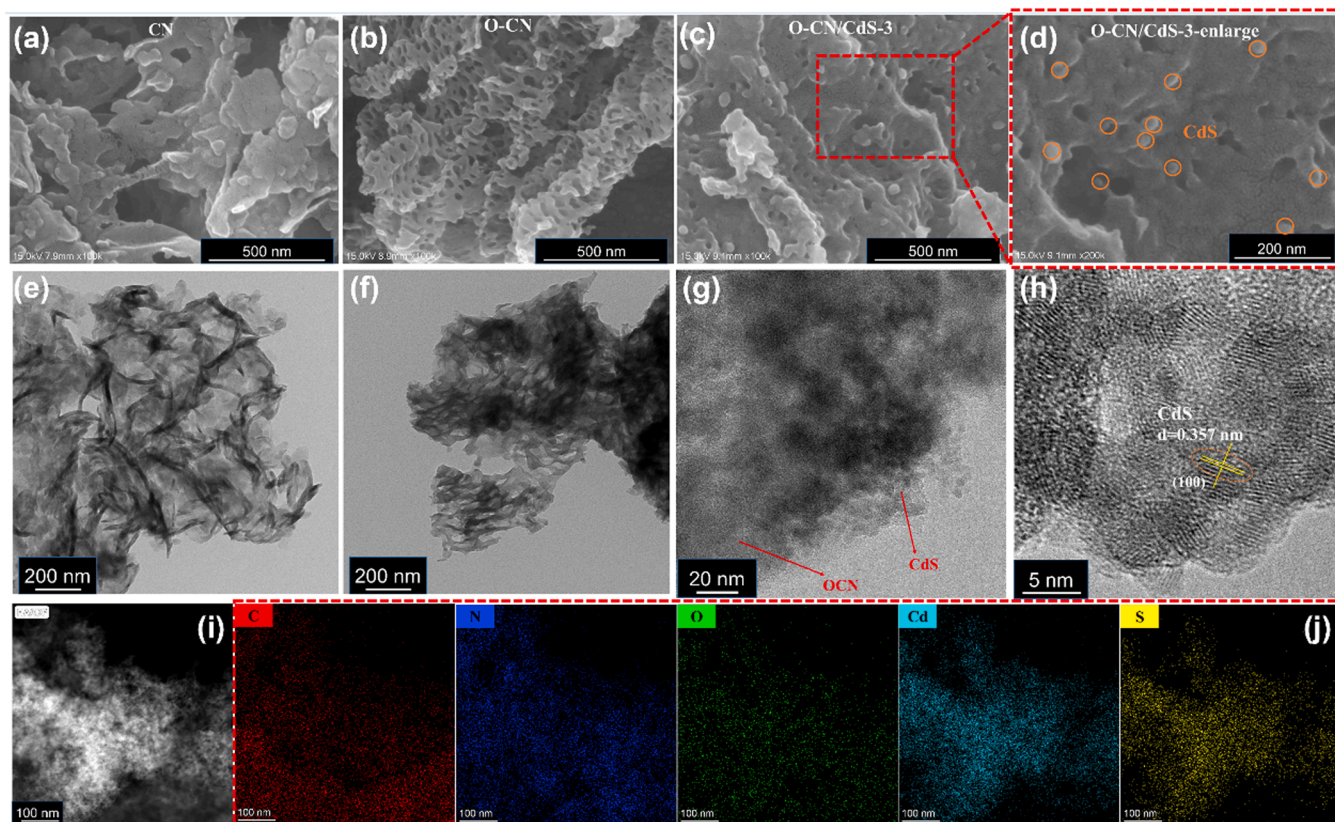
Fig. 1. The SEM images of (a) CN, (b) O-CN, (c) O-CN/CdS-3, and (d) enlarged SEM images of O-CN/CdS-3; The TEM images of (e) CN, (f) O-CN, (g) O-CN/CdS-3, (h) HRTEM images of O-CN/CdS-3, (i) HAADF image and (j) elemental mapping of O-CN/CdS-3.

$$Removal\ rate(\%) = \left(1 - \frac{C_t}{C_0}\right) \times 100\%$$

C_t is the concentration of CPs at time t, C_0 means the initial concentration of CPs. All the experiments were conducted triplicate.

3. Results and discussion

3.1. Schematic overview and mechanism of the Z-scheme O-CN/CdS heterostructure

As shown in Scheme 1, O-doped g-C₃N₄ (O-CN) was prepared via calcination. The Zeta potential of O-CN in deionized water was measured as − 15.3 mV (Fig. S2), indicating that the surface of O-CN was negatively charged. Then, CdS was loaded onto O-CN via an in-situ hydrothermal method, and O-CN/CdS samples with different component content were successfully synthesized, the detailed synthesis of which can be found in the Supplementary Material.

3.2. Morphology, structure, and composition of the photocatalysts

#### 3.2.1. Morphology characterization of the photocatalysts

Morphologies of the samples were analyzed by scanning electron microscopy (SEM) and transmission electron microscopy (TEM). CN exhibited a layered and stacked 2D structure with uneven surfaces and randomly distributed mesoporous pores (Fig. 1a and e). Fig. 1b, f showed that, upon O-doping, the resulting O-CN featured a large number of holes due to the gas produced in the reaction process, which acted as active sites to promote mass transfer and photocarrier separation. Fig. 1c, d, and Fig. S3 showed SEM images of O-CN/CdS materials with varying CdS content (3%, 5%, 7%, and 9%), where CdS NPs of around 20 nm in diameter are loaded on the O-CN. At first, CdS NPs were uniformly dispersed on the O-CN. With the increase of the CdS loading amount, CdS nanoparticles appeared to aggregate. To observe the combination of CdS NPs and O-CN, Fig. 1g showed a partially enlarged image of OCN/CdS-3, in which some CdS NPs can be observed to be attached to O-CN, forming a tight contact layer. The high-resolution TEM (HRTEM) image (Fig. 1h) of OCN/CdS-3 exhibited a lattice fringe of 0.357 nm, which corresponded to the (100) crystal plane of CdS [25]. Furthermore, elemental mapping and energy-dispersive X-ray spectroscopy (EDS) mapping measurements showed that the C, N, O, Cd, and S elements were uniformly distributed in OCN/CdS-3 (Fig. 1j and Fig. S4), confirming the successful preparation of an OCN/CdS heterojunction.

3.2.2. Characterisation of the structure and composition of the photocatalysts

The phase structures of g-C₃N₄, O-CN, CdS, and O-CN/CdS-x were determined via X-ray diffractometry (XRD) measurements. In Fig. 2a, the XRD pattern of g-C₃N₄ (JCPDS 50–1250) featured two dominant peaks at 13.3° and 27.4° that can be attributed to the (100) and (002) crystal planes, corresponding to the in-plane tri-s-triazine units and the periodic stacking of conjugated aromatic systems, respectively [26]. The diffraction pattern of O-CN was roughly similar to that of CN, revealing that the original crystal structure of CN was retained in O-CN and was basically unchanged after the doping of CN with O. Further comparison of the differences in crystal structure between O-CN and CN, as shown in the XRD patterns in Fig. S5, the (002) crystal plane of O-CN was shifted to the left, indicating that the interlayer distance increased from 3.26 Å to 3.30 Å due to the change in the interlayer structure of the O-doped polymer. Moreover, the broadening of the (002) crystal plane diffraction peak indicated a reduction in the crystal size of the polymer [14]. No obvious characteristic diffraction peaks of CdS were observed in the XRD pattern of O-CN/CdS, indicating the high dispersion of CdS in the
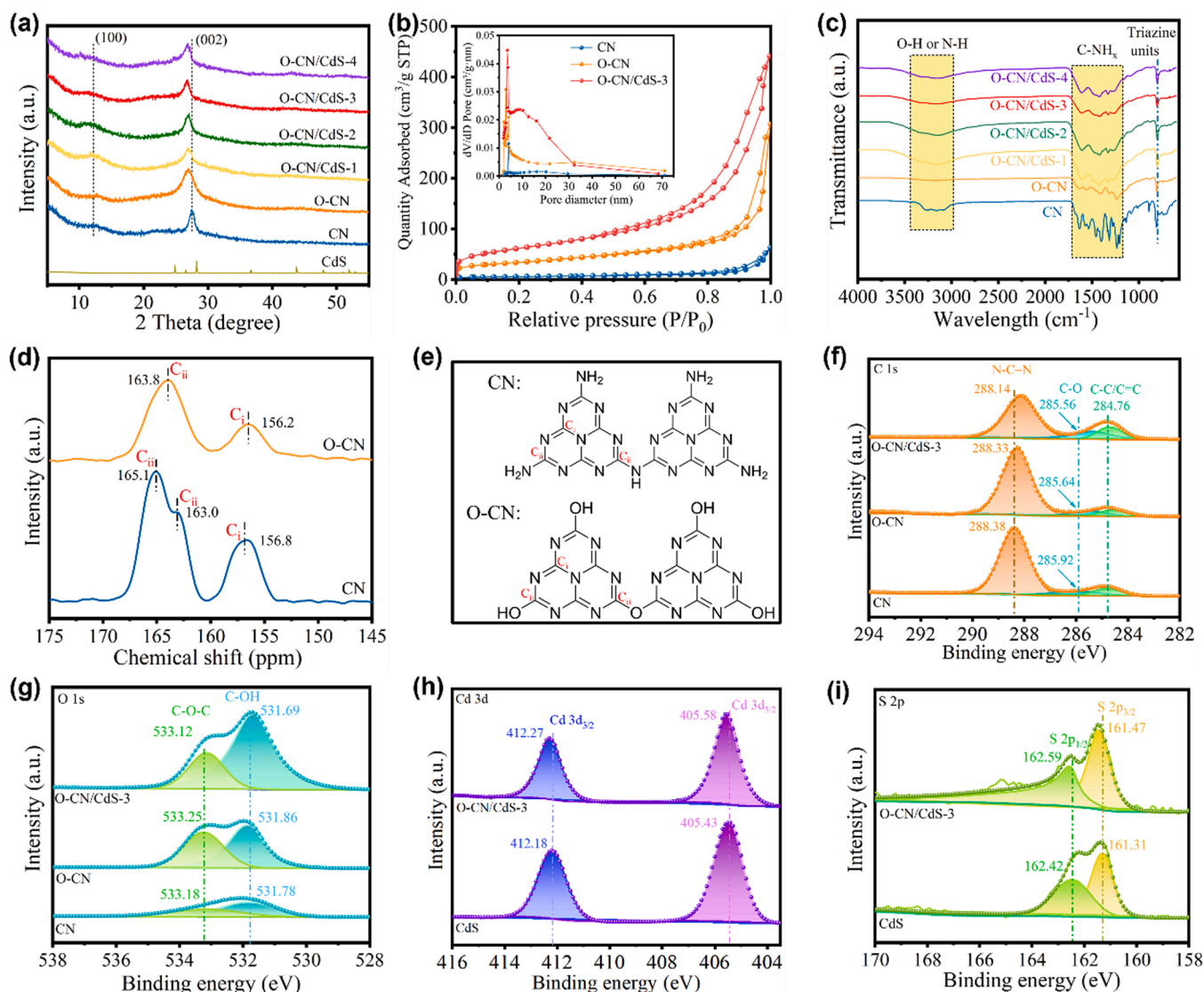
Fig. 2. (a) XRD patterns of CdS, CN, O-CN, and O-CN/CdS-x. (b) N_2 adsorption/desorption isotherms and corresponding pore-size distribution curves (inset). (c) FT-IR spectroscopy of CN, O-CN, and O-CN/CdS-x. (d) ^{13}C solid-state nuclear magnetic resonance (ssNMR) and (e) corresponding structural formula of CN and O-CN. High-resolution XPS spectra of (f) C 1 s, (g) O 1 s, (h) Cd 3d, (i) S 2p.

composite material. The (002) diffraction peak of O-CN/CdS-3 shifted slightly to the left, revealing that the O-CN interlayer distance increased due to the introduction of CdS, confirming that CdS was successfully doped between O-CN layers during the recombination process [25]. CdS interspersed between O-CN layers to form O-CN/CdS heterojunction that promoted charge separation and enhanced photocatalytic activity compared to its individual components.

In Fig. 2b, Nitrogen adsorption-desorption measurements were conducted to evaluate the BET (Brunauer–Emmett–Teller) surface areas and pore size distributions of the as-prepared samples. As listed in Table S1, CN had the lowest BET surface area (20.2263 $m^2\ g^{-1}$) and pore volume (0.097382 $cm^3\ g^{-1}$). However, after the introduction of O atoms, the BET surface area and pore volume of CN increased to 118.6855 $m^2\ g^{-1}$ and 0.474208 $cm^3\ g^{-1}$, respectively. These results indicated that the O atoms doping had a significant effect on the pore size distribution of CN, thus increasing its BET surface area, which was consistent with the SEM results. After loading O-CN with CdS NPs, the O-CN/CdS-3 sample exhibited an increased BET surface area (221.1306 $m^2\ g^{-1}$), providing abundant active sites and facilitating the mass transfer process during the photodegradation of 2-CP.

Fourier transform infrared spectroscopy (FT-IR) measurements were

tested to determine the changes to the chemical structure of O-CN/CdS. In the spectra of Fig. 2c, for CN and O-CN, the characteristic absorption of the tri-s-triazine ring is at 810 cm^{-1}, and the absorption peaks at 1200–1600 cm^{-1} corresponded to the stretching vibration of the C–N heterocyclic ring, and the peaks in the range of 3000 – 3300 cm^{-1} can be assigned to NH_x. Besides this, the spectrum of O-CN showed an additional peak at 3340 cm^{-1}, attributed to –OH groups [27]. In contrast, the FT-IR spectra of the O-CN/CdS composites were similar to that of O-CN, confirming that O-CN had successfully incorporated into the O-CN/CdS photocatalysts.

^{13}C solid-state nuclear magnetic resonance (ssNMR) spectra was recorded to investigate the structural changes of CN after its doping with O atoms. In Fig. 2d, the ^{13}C ssNMR spectrum of CN showed three peaks at 156.8, 163.0, and 165.1 ppm, which can be assigned to three types of carbon environments in N-linked heptazine, C_iN_3, $C_{ii}N_2NH_2$, and $C_{ii}N_2NH$, respectively. Moreover, the spectrum of O-CN also featured three types of carbon environments: C_iN_3, N_2-C_{ii}-OH, and N_2-C_{ii}-O. The C_{ii} peaks of O-linked heptazine (O-CN) were merged into one signal and are located between those of N-linked heptazine, which was consistent with the ^{13}C ssNMR spectrum of O-CN, which featured two peaks at 156.2 and 163.8 ppm. This suggested that O-CN comprised both N- and
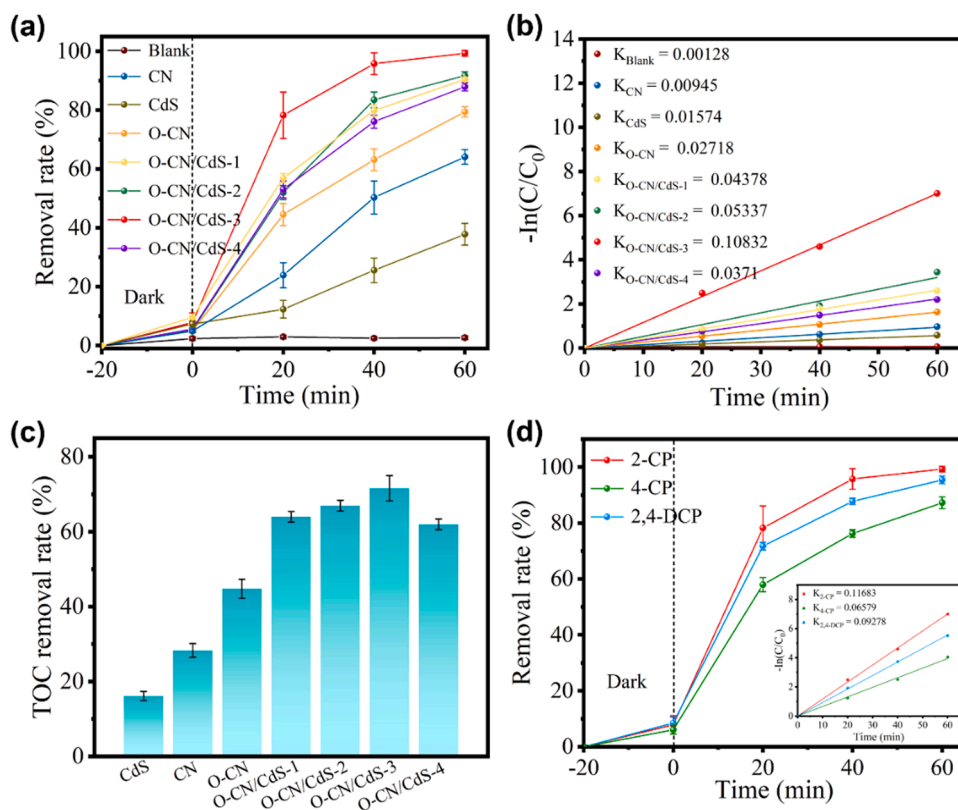
Fig. 3. (a) Photodegradation of 2-CP by different samples, (b) pseudo-first-order kinetics curves of 2-CP degradation; (c) The TOC removal rates of 2-CP by different samples; (d) Degradation of three CPs (2-CP, 4-CP, and 2,4-DCP), and corresponding kinetic constants (inset). Conditions: [pollutant]$_0$ = 10 mg/L, [Cat.] = 0.7 g/L, ambient temperature, no buffer.

O-linked heptazine. Besides this, the O-doping of CN led to the chemical shift of C$_{ii}$ to a lower value, indicative of an N linker being replaced by the terminal and bridged O atoms [14]. These results were consistent with the proposed structural formula of O-CN (Fig. 2e).

Moreover, the detailed chemical compositions and electronic structures of the photocatalysts were investigated by X-ray photoelectron spectroscopy (XPS). In Fig. S6a, the signals of C, N, and O elements existed in both CN and O-CN. The C 1 s spectrum (Fig. 2f) of O-CN showed three main peaks at 284.76, 285.56, and 288.14 eV, attributed to adventitious carbon species, C–O bonding, and the sp^2 hybridized carbon of the triazine rings (N–C=N) [28]. In the N 1 s spectrum of O-CN (Fig. S6b), three peaks were located at 398.56, 399.39, and 400.63 eV, ascribed to C–N = C, N–C$_3$, and N–H, respectively [27]. The decreased intensity of the N–C$_3$ peak in the spectrum of O–CN on account of the replacement of N–C$_3$ bonds with C–O bonds (Fig. 2g). In Fig. S6a, the survey XPS spectra of O-CN/CdS indicated the presence of C, N, O, Cd, and S in the photocatalysts, consistent with the EDS mapping results, thus indicating the O-CN/CdS heterojunction was successfully prepared. As shown in Fig. 2h-i, the peak positions of 405.58 and 412.27 eV corresponding to Cd 3d$_{5/2}$ and Cd 3d$_{3/2}$, respectively, and thus the state of Cd^{2+} is confirmed [25]. Analogously, the S 2p spectrum shows two peaks located at 161.47 and 162.59 eV, assigning to the S 2p$_{3/2}$ and S 2p$_{1/2}$ of S^{2-}, respectively. For O-CN/CdS-3, the binding energies of the sp^2 hybridized carbon of the triazine rings (N–C=N) and C–N = C exhibited a positive shift of around 0.08 – 0.18 eV compared to those of O-CN, while the peaks of Cd 3d and S 2p displayed a negative shift compared to those of pure CdS (Fig. 2h and i). These peak shifts indicated that charges transfer between CdS and O-CN in the heterojunction [29]. These results suggested that the introduction of O atoms changes the electronic structure of CN, with strong chemical interactions forming in the O-CN/CdS heterojunction, thus promoting electron migration between CdS and O-CN.

3.3. Photocatalytic performance

3.3.1. Comparison of synthesized samples

The photocatalytic performances of the O-CN/CdS photocatalysts towards 2-CP degradation were evaluated under a 300 W Xenon (Xe) lamp (λ = 420–800 nm). Fig. S7 shows the dark-adsorption stage, all samples reached adsorption equilibrium within 30 min. Among them, the O-CN/CdS-3 (9.3%) showed better adsorption abilities than CN (4.4%) and O-CN (6.9%), which may be attributed to its relatively large surface area (Fig. 2b). Under visible-light irradiation, CN exhibited poor photocatalytic activity, possessing a removal rate of only 60.4% of 2-CP from solution within 60 min, owing to the rapid recombination of photogenerated charges. In comparison, after O-doping the 2-CP photodegradation rate of O-CN increased to 77.8% within 60 min, indicating that O-doping hindered the recombination of photogenerated electron holes to some extent and polished up the photocatalytic performance of CN. The photocatalytic activity of O-CN and CdS were further enhanced after their formation of the heterojunction O-CN/CdS. Moreover, with an increase in the CdS content, the 2-CP removal rate first increased and then decreased, among them, O-CN/CdS-3 showed the highest reduction rate of 100% within 60 min of the O-CN/CdS photocatalysts. This suggested that with an increase in the CdS NPs content that the composite O-CN/CdS material shows effective charge separation. However, an excess of CdS in O-CN/CdS hinders the electron transport orbit of O-CN. In addition, the high accumulation of CdS NPs reduced the specific surface area of the O-CN/CdS composite materials, thus leading to them exhibiting reduced light absorption efficiency. Next, the photocatalytic efficiency of 2-CP by O-CN/CdS-3 at monochromatic wavelengths (380, 400, 420, 450, 500, 550, 600 and 700 nm) was measured. Fig. S9 shows the apparent quantum efficiency (AQE) versus wavelength plot, together with the UV–vis absorption spectrum of O-CN/CdS-3. The calculated AQE results (Table S3) revealed that the
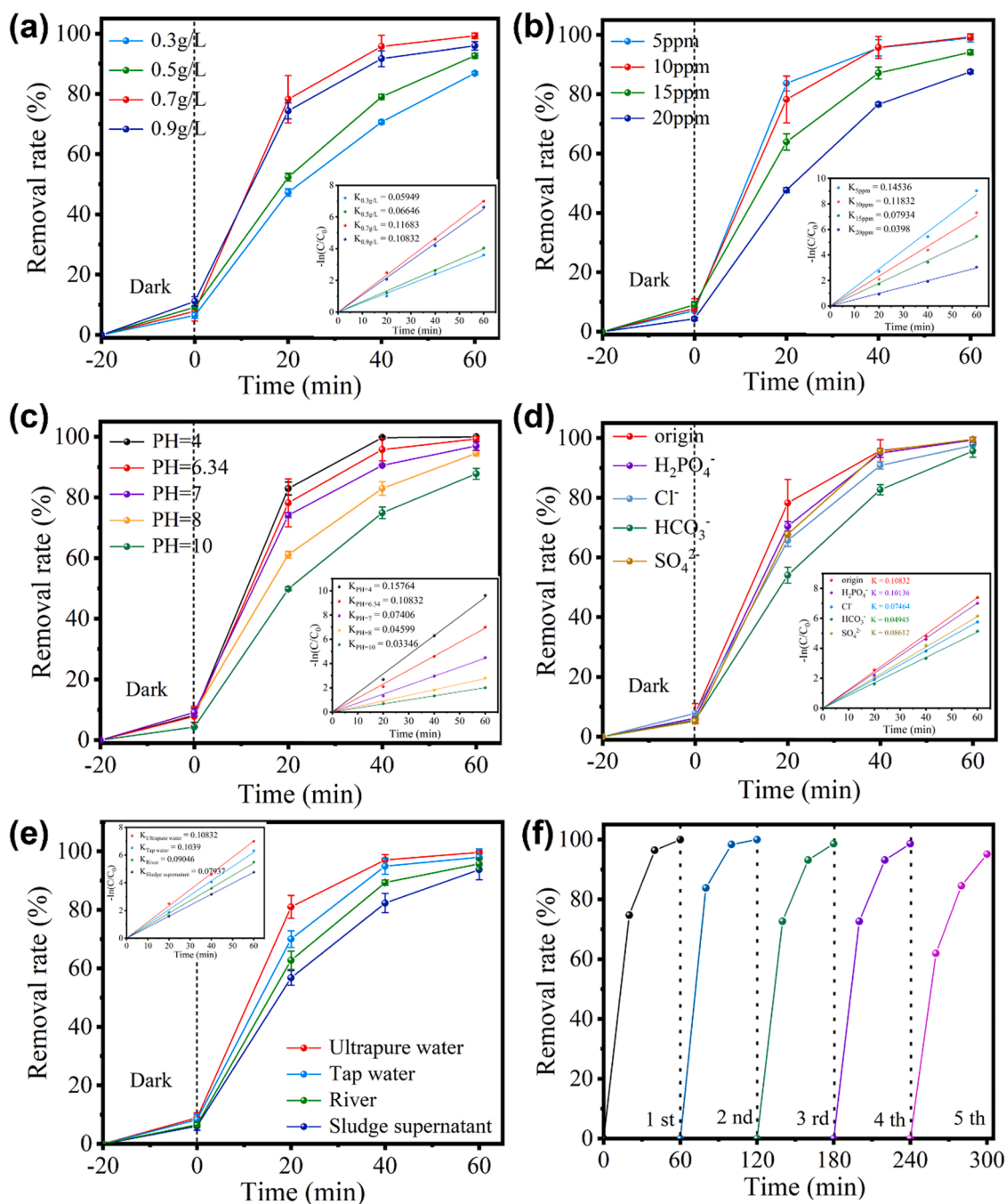
Fig. 4. (a) Degradation of 2-CP under different O-CN/CdS-3 loading, and corresponding kinetic constants (inset); (b) Degradation of 2-CP with different concentrations, and corresponding kinetic constants (inset); (c) Degradation of 2-CP under different pH values, and corresponding kinetic constants (inset); (d) Degradation of 2-CP in the presence of different inorganic ions ($H_2PO_4^-$, Cl^-, SO_4^{2-}, and HCO_3^-), and corresponding kinetic constants (inset); (e) Degradation of 2-CP from different water sources, and corresponding kinetic constants (inset); (f) Reusability of O-CN/CdS-3 after degradation of 2-CP.

degradation of the 2-CP reaction was inducted via light absorption by the photocatalyst. We also conducted total organic carbon (TOC) measurements to study the mineralization rate of 2-CP. In Fig. 3c, the mineralization rate of O-CN/CdS-3 under visible light was 72%, which was better than those of both O-CN and CdS. However, the photocatalytic degradation efficiency of O-CN/CdS-3 was 100%, with the difference between the degradation rate and mineralization rate attributed to the longer time required for mineralization of the intermediate. Then, the efficiency of O-CN/CdS-3 towards the degradation of chlorophenols (2-CP, 4-CP, and 2,4-DCP) was investigated to study the universality of its application. As shown in Fig. 3d, the degradation rates of all of the CPs were > 80% within 60 min, indicating that O-CN/CdS-3

showed good versatility for treating CP-containing wastewater. Hence, O-CN/CdS-3 exhibited excellent performance, comparing the above results to other similar recent works (Table S4).

3.3.2. Effects of different external factors on photocatalysis

In Fig. 4a, the influence of initial catalyst dosage on the degradation of 2-CP was investigated. Initially, the photocatalytic efficiency improved gradually with an increase in the catalyst dosage, revealing an increase in active sites of the photocatalyst. At a catalyst dosage of 0.7 g/ L, the degradation rate of O-CN/CdS-3 reached a maximum. After this point, with a further increase in catalyst concentration, there were no significant changes in photocatalytic efficiency, and the reaction
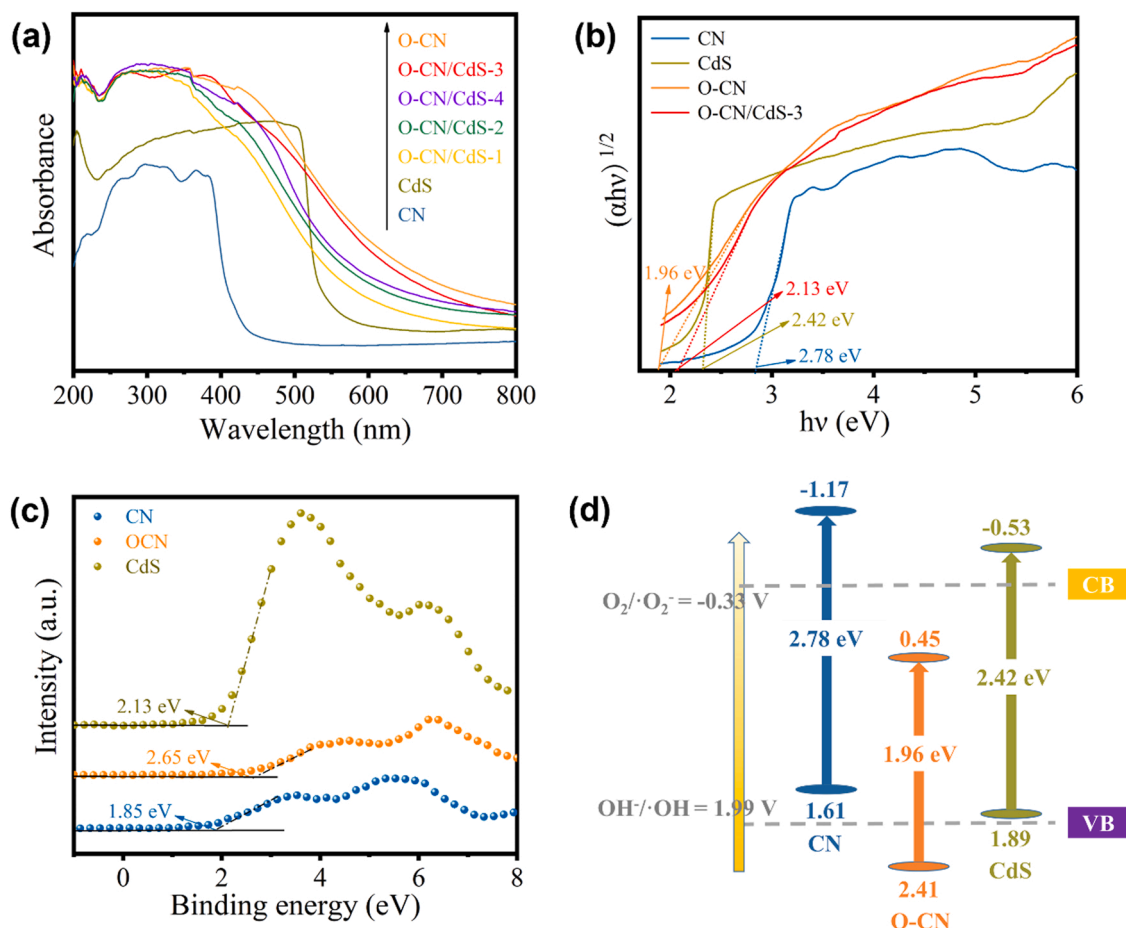
Fig. 5. (a) UV–VIS diffuse reflectance spectra (DRS), (b) band gap energies; (c) XPS valence band spectra; (d) Band structures of CN, O-CN, and CdS.

efficiency reached an extreme value or even slightly decreased. This indicated that excess catalyst made the solution turbid, hindering the absorption of light and reducing photocatalytic efficiency [30]. The influence of different initial concentrations of 2-CP on the degradation efficiency of the photocatalyst was shown in Fig. 4b. Upon a decrease in the concentration of 2-CP from 20 ppm to 5 ppm, there was a 3.7-fold increase in the reaction rate constant, which conformed to a first-order kinetics process. When the catalyst content remained constant and the number of reaction sites was fixed, the removal rate decreased with an increase in the reactant concentration.

To explore the effect of pH on photocatalytic efficiency, 2-CP was photocatalytic degraded at different pH values (4, 6.34, 7,8, and 10). In Fig. 4c, the photodegradation of 2-CP under acidic conditions was obviously better than that under alkaline conditions, therefore indicating that pH affected the interaction between the pollutants and photocatalyst. Under alkaline conditions, an excess of hydroxide ions in the system increased the electrostatic repulsion between the pollutants and photocatalyst, reducing the photocatalytic efficiency. In contrast, under acidic conditions, 2-CP existed in a molecular state and combines with the photocatalyst via van der Waals forces. In addition, pH also affected the activity of free radicals involved in the degradation of pollutants. Under acidic conditions, $\cdot O_2^-$ tended to generate hydrogen peroxide (H_2O_2) with photogenerated holes to promote photocatalytic degradation [31]. With an increase in pH, the photogeneration of holes was inhibited, thus impeding the photocatalytic reaction process. Therefore, the formation of some active species, such as photogenerated holes and $\cdot O_2^-$, are not easily inhibited under certain acidic conditions, therefore meaning that 2-CP can be degraded more efficiently.

In real-world applications, inorganic anions are present in sewage

alongside pollutants. Thus, some common metal sodium salts (10 mmol/L), including $H_2PO_4^-$, Cl^-, SO_4^{2-}, and HCO_3^- were added to the reaction solution to investigate their effect on the photodegradation of 2-CP. In Fig. 4d., the inhibitory effect of $H_2PO_4^-$, Cl^-, and SO_4^{2-} were not obvious attributed to their being adsorbed on the surface of the catalyst and cannot shield the active site of the photocatalytic. Nevertheless, HCO_3^- slightly inhibited the photocatalytic activity of the O-CN/CdS-3 photocatalyst, due to HCO_3^- capturing active species during the photocatalytic reaction process [32]. These results thus indicated that the O-CN/CdS-3 heterojunction exhibited excellent anti-interference ability in an environment containing inorganic anions.

Water quality is a significant index of photocatalytic degradation efficiency in real wastewater treatment [33]. We explored the photodegradation efficiency of O-CN/CdS-3 towards 2-CP in samples of water from different sources, including ultrapure water, tap water, water from Soochow University River, and sludge supernatant. The water quality parameters of the different samples were listed in Table S2, including those of inorganic cations and organic matter. Among these, the COD of the sludge supernatant is the highest (75 mg/L), while the concentrations of inorganic cations were roughly similar. In Fig. 4e, the photocatalytic performance of O-CN/CdS-3 towards the samples from different water sources followed the order of ultrapure water > tap water > Soochow University River > sludge supernatant, while the maximum inhibition did not reach 15%. Due to most of the inorganic anions playing a slight role in the photodegradation progress of O-CN/CdS-3 (Fig. 4d), the decreased photodegradation rate of O-CN/CdS-3 in sludge supernatant may be due to the co-existing organic compounds competing with 2-CP for the photocatalytic reaction sites on O-CN/CdS-3. These results revealed that O-CN/CdS-3 exhibits universal
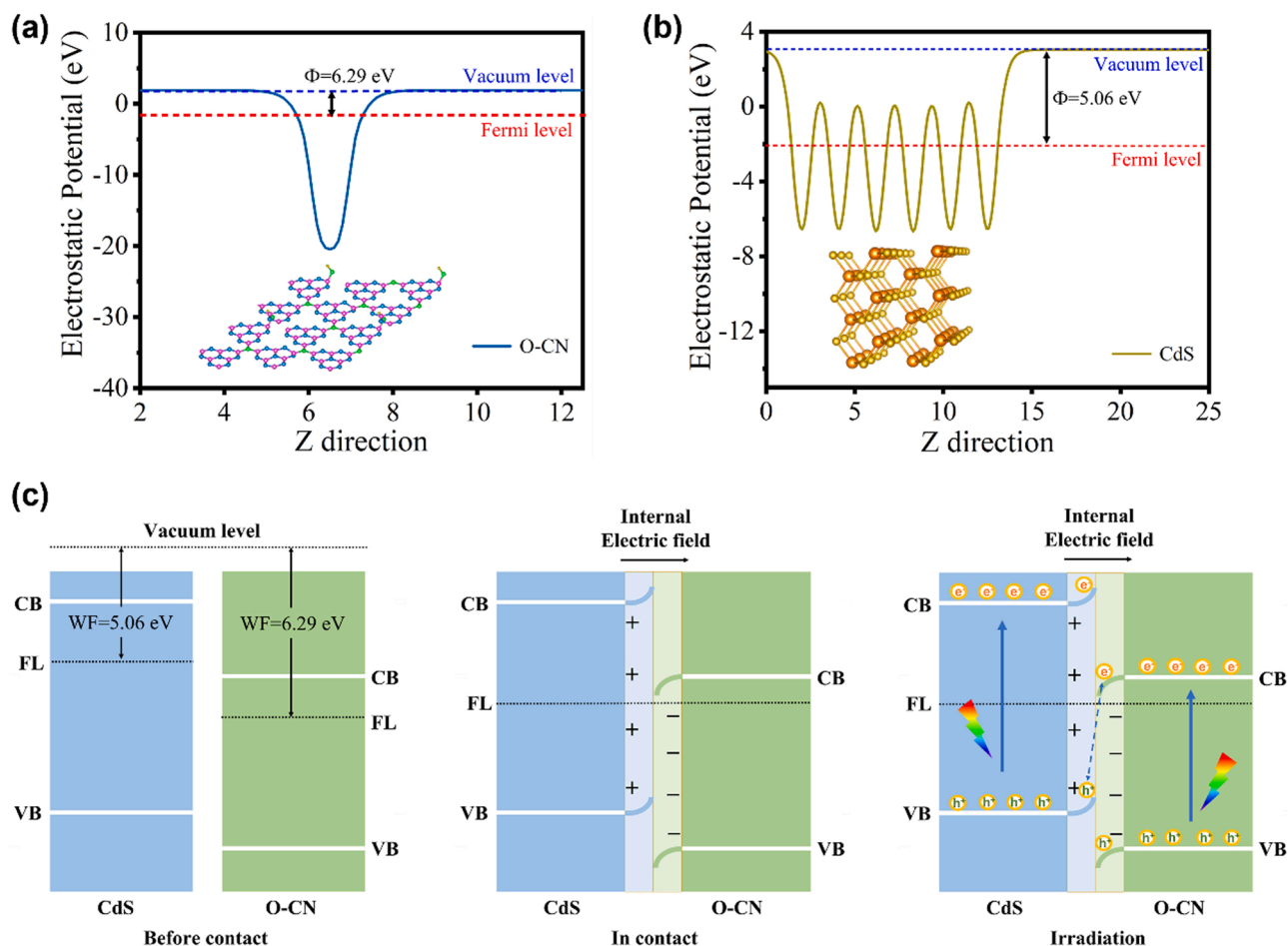
Fig. 6. DFT calculated electrostatic potentials diagrams for (a) O-CN and (b) CdS (100) surface; (c) Schematic band diagram and interfacial charge properties of the O-CN/CdS heterostructure. WF, work function; FL, Fermi level.

applicability in water from different sources.

3.3.3. Reusability

The reusability of O-CN/CdS-3 was also measured by conducting cycling tests. In Fig. 4f, the degradation rate of O-CN/CdS-3 did not obviously decrease after five cycles, with the 2-CP photodegradation rate of > 90% still observed in the fifth run. In Fig. S10, the XRD spectra and SEM images of O-CN/CdS-3 before and after its reaction showed no obvious differences. Chemical state changes of the O-CN/CdS-3 before and after reactions were also investigated by XPS (Fig. S11). No obvious peak shift in OCN/CdS-3 after five cycles was observed, proving the outstanding stability of the composite photocatalysts. These results suggested that the composite photocatalyst exhibited excellent reusability and is safe.

3.4. Photodegradation mechanisms

3.4.1. Optical characteristics and band structure

Ultraviolet-visible (UV–vis) diffuse reflectance spectroscopy was used to analyze the optical properties of the photocatalysts, and XPS valence band spectra were tested to explore the band structure of the heterojunction, the results of which are shown in Fig. 5a. Obviously, the light absorption edge of CN was < 450 nm and that the light absorption range of O-CN after O-doping extended across the entire visible region of the electromagnetic spectrum. The absorption peak of CdS was at around 570 nm, but the optical absorption edge moved to a longer wavelength after the loading of O-CN, revealing that the introduction of O-CN broadened the visible-light response range of the O-CN/CdS

composite. The bandgap of CN, CdS, O-CN, and O-CN/CdS-3 were calculated using the Kubelka–Munk equation (Eq. 1):

$$(\alpha h\nu)^{n/2} = A \, (h\nu - E_g)) \tag{1}$$

where n was specific to the semiconductor type. The calculated band gaps of CN, CdS, O-CN, and O-CN/CdS-3 were 2.78 eV, 2.42 eV, 1.96 eV, and 2.13 eV, respectively (Fig. 5b). Valence band (VB)-XPS spectra (Fig. 5c) were recorded to further analyze the VB position. Measurement errors were eliminated according to the following equation (Eq. 2):

$$VB \, (vs \cdot NHE) = \Phi + VB_{XPS} - 4 \cdot 44 \, eV \tag{2}$$

where Φ (4.2 eV) and 4.44 eV corresponded to the work function of the XPS analyzer and the vacuum level [34], respectively. The VB positions (vs. NHE) of CN, O-CN, and CdS were determined to be 1.61 V, 2.41 V, and 1.89 V, respectively. Therefore, using the following equation, $E_g = E_{VB} - E_{CB}$, the calculated conduction band (CB) potentials of CN, O-CN, and CdS were − 1.17 V, 0.45 V, and − 0.53 V versus NHE, respectively (Fig. 5d), which roughly matched the information measured from Mott–Schottky plots (Fig. S8).

3.4.2. Density functional theory (DFT) calculation

DFT was used to explore the charge transfer pathway at the heterojunction interface [35]. The work functions (Φ) of O-CN and CdS were figured out according to Eq. (3):

$$\Phi = E_{vac} - E_F \tag{3}$$

where E_{vac} represented the vacuum level and E_F was the value of the
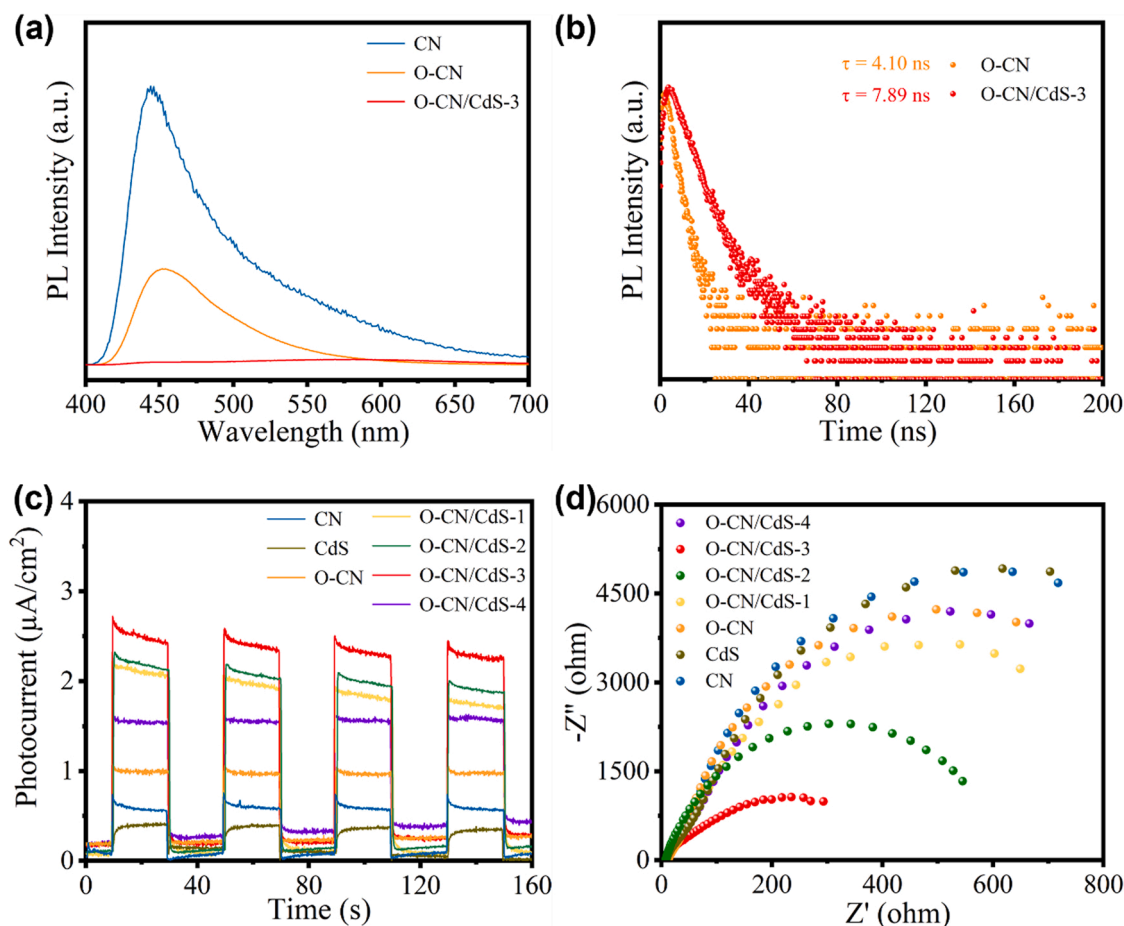
Fig. 7. (a) photoluminescence (PL); (b) TRPL spectra; (c) photocurrent response (I-t); (d) Electrochemical impedance spectra (EIS).

Fermi level. As shown in Fig. 6a and 6b, O-CN (6.29 eV) exhibited a higher work function than CdS (5.06 eV), indicating that the Fermi level of O-CN was lower than that of CdS. Thus, when CdS and O-CN came into contact, the electrons were more likely to migrate from CdS to O-CN to achieve Fermi level equilibrium. Meanwhile, the heterojunction interface formed a built-in electric field from CdS to O-CN, which thus greatly promoted interfacial carrier separation. Due to the high Fermi level of CdS, its energy bands bent upward at the interface, while the energy bands of O-CN with a low Fermi level bent downward. Consequently, the photogenerated electrons on the CB of O-CN tended to transfer to the VB of CdS and recombine with the photogenerated holes (Fig. 6c). According to the above analysis, the charge transfer pathway was thought to follow a direct Z-scheme mechanism.

3.4.3. Enhanced charge separation and transfer kinetics

Kelvin probe force microscopy (KPFM), photoluminescence (PL) emission spectroscopy, time-resolved PL (TRPL) spectra, surface photovoltage (SPV) spectra and photoelectrochemical characterizations were further used to explore the electronic transfer pathway between CdS and O-CN. Fig. S13a and S13e display the topographic images of O-CN and O-CN/CdS-3, respectively. In Fig. S13b-d, the surface potentials of O-CN before and after illumination changed not obviously, indicating rapid charge carrier recombination. The surface potential distribution of O-CN/CdS-3 showed in Fig. S13e-h, a higher surface potential of CdS than that of O-CN could be clearly observed, revealing the interface formed a built-in electric field from CdS to O-CN. After irradiation, the surface potential of CdS (ΔCPD = −390 mV) decreased due to the transfer of electrons under the built-in electric field, meanwhile the surface potential of O-CN (ΔCPD = 310 mV) increased arise from the consumed electrons. As shown in Fig. 7a, the PL intensity of CN was

much stronger than that of O-CN, indicating the low rate of photogenerated carrier recombination after O-doping. Importantly, the PL intensity of the O-CN/CdS composites further decreased, indicating that the introduction of CdS can effectively inhibit the hole-electron recombination of O-CN, which favoured the transfer of photogenerated carriers. Among them, O-CN/CdS-3 exhibits the weakest emission peak (Fig. S14a), which is consistent with its optimal photocatalytic degradation of 2-CP. Therefore, we further confirmed the result by SPV spectra (Fig. S14b), which showed that the OCN/CdS-3 possessed a higher SPV signal than that of the separated O-CN and other hybrids. In Fig. 7b, time-resolved PL spectroscopy was performed to study the average lifetimes of O-CN and O-CN/CdS-3, with the average lifetime of O-CN/CdS-3 (7.89 ns) being longer than that of O-CN (4.10 ns). This indicated that the photogenerated charges of O-CN/CdS-3 tended to take part in the subsequent catalytic reaction and promote its photocatalytic performance [36]. As shown in Fig. 7c and d, photocurrent response curves (I– T) and electrochemical impedance spectroscopy (EIS) were tested to corroborate the separation–migration behaviour of the photocatalysts. From the data, it can be seen that the photocurrent density of O-CN was higher than that of CN, indicating its excellent charge separation efficiency. This revealed that the O-doping of CN promotes its charge separation efficiency. The photocurrent density of O-CN/CdS-3 was the highest among all the photocatalysts, suggesting that it exhibited the highest charge transfer rate, thus further confirming the formation of the Z-scheme heterojunction [37]. Electrochemical impedance spectroscopy (EIS) data were recorded that show the same result, with O-CN/CdS-3 exhibiting the smallest semicircle among all the samples, indicating it exhibited the lowest charge transfer resistance, meaning that it tended to promote the transfer of charges [38]. These suggested that the construction of an O-CN/CdS
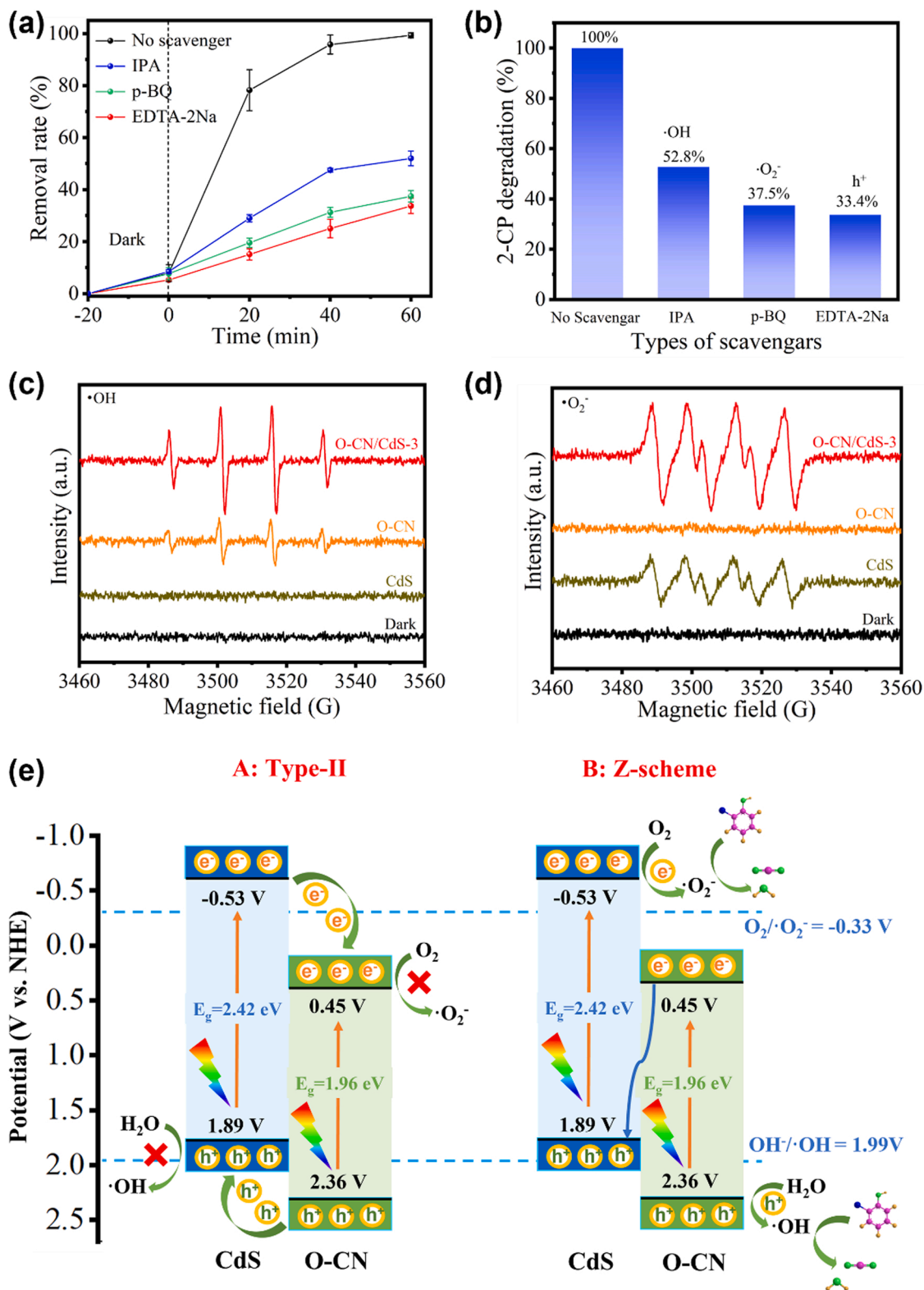
Fig. 8. (a) 2-CP removal rates of O-CN/CdS-3 with different scavengers and (b) the effect of corresponding radicals on the 2-CP degradation. ESR spectrum of (c) DMPO-·OH adduct, (d) DMPO-·O_2^- adduct. (e) The photocatalytic mechanisms of the Z-scheme O-CN/CdS-3.

heterostructure enhanced the migration rate of photogenerated charges, which improved the photocatalytic performance of O-CN/CdS towards its degradation of CPs.

3.4.4. Radical quenching experiments and mechanism of Z-scheme heterojunction

Radical quenching experiments were further studied to explore the active species in photodegradation. In the radical quenching experiments of O-CN/CdS-3, p-benzoquinone (p-BQ), ethylenediaminetetra-acetate (EDTA-2Na), and isopropyl alcohol (IPA) were used to

capture·O_2^-, holes (h$^+$), and ·OH, respectively [39]. As shown in Fig. 8a and b, upon adding P-BQ and EDTA-2Na to the photocatalytic reaction, there was a significant decrease in the photodegradation rate of 2-CP, indicating that ·O_2^- and h$^+$ were the main active species. Meanwhile, the addition of IPA led to 52.8% inhibition in the degradation of 2-CP, indicating that ·OH also played an active role in the photodegradation of 2-CP. Fig. 8c and d showed the ESR spectra of the reactions that feature strong signals for ·O_2^- and ·OH, which was consistent with the results of radical quenching experiments, confirming that ·O_2^- and ·OH are both active free radicals in the photocatalysis reaction.

Band structure matching is the key to forming an excellent Z-scheme heterojunction photocatalyst [7]. Above all characterization and photocatalytic experimental results, the mechanism of the photocatalytic reaction of the O-CN/CdS heterostructure was speculated to be type-II or Z-scheme heterojunction in nature. It was thus assumed that the photocatalytic mechanism of the O-CN/CdS photocatalyst proceeds via a type-II heterojunction. In Fig. 8e-A, electrons transferred from the CB of CdS to the CB of O-CN, and the holes in the VB of O-CN transferred to the VB of CdS, thus facilitating carrier separation to a certain extent. In this case, as the VB of CdS was more negative than OH$^-$/·OH (1.99 V vs. NHE) and the CB of O-CN was more positive than O_2/·O_2^- (−0.33 V vs. NHE), the holes in the VB of CdS cannot oxidize OH$^-$ to produce·OH and the electrons in the CB of O-CN cannot reduce O_2 to ·O_2^-. Moreover, according to the ESR analysis that showed that both ·O_2^- and·OH were the key active free radicals in the reaction, a traditional type-II photocatalytic mechanism may not apply to the O-CN/CdS heterojunction. According to the above analysis, a Z-scheme heterojunction mechanism was proposed, as shown in Fig. 8e-B. Following the Z-scheme heterojunction charge transfer pathway, the electrons in the CB of O-CN transferred and recombined with the holes in the VB of CdS under visible light. The photocatalysis system showed strong photoelectron reducibility of the CdS CB and strong hole oxidisability of the O-CN VB to generate both ·O_2^- and·OH radicals, which was consistent with the ESR results.

3.4.5. Possible degradation pathway of 2-CP

Subsequently, ion chromatography (Lcs-1100) was used to detect the Cl$^-$ concentration in 2-CP solution during photocatalytic reactions. As shown in Fig. S15, the concentration of Cl$^-$ concentration in 2-CP solution gradually increased to 58.28 μM as the reaction continued, which may be attributed to the triggered dechlorination of 2-CP by the active free radicals. While the detected concentration of Cl$^-$ was lower than theoretical value (77.78 μM). Next, XPS characterization was used to analyze O-CN/CdS-3 after the reaction to explore the presence of the remaining Cl$^-$. High-resolution XPS spectra of Cl 2p showed the presence of Cl$^-$ ions on the O-CN/CdS-3 surface (Fig. S16), indicating that O-CN/CdS-3 had dechlorination abilities. To further elucidate the possible degradation pathway of 2-CP, liquid chromatography-mass spectrometry (LC-MS) was used to identify the main intermediate products in the photodegradation process. Fig. S9 exhibited the total ion chromatogram of the reaction. The reaction commenced with only one peak (A: $m/z = 128.8$) corresponding to 2-CP, which after 30 min decreased obviously and formed a series of new peaks ((B: $m/z = 93.4$), (F: $m/z = 145.8$), (G: $m/z = 109.8$), and (H: $m/z = 109.8$)), implying the preliminary decomposition of 2-CP and the formation of a series of intermediate products. Above intermediate products analysis, it can be inferred that only dechlorination and hydroxylation occurred in the first 20 min of the reaction, with no damage occurring to the benzene ring structure of 2-CP. When the reaction time at 40 min, the weak peak of 2-CP indicated the outstanding photodegradation performance and appeared some peaks ((C: $m/z = 107.3$), (D: $m/z = 115.8$), (E: $m/z = 88.5$), (I: $m/z = 140.8$), and (J: $m/z = 59.2$)) of smaller molecular weight. According to the above intermediate products, it was inferred that the benzene ring of 2-CP was opened in the second half of the reaction. The degradation pathway of 2-CP was thus thought to be mainly separated into dechlorination, ring-opening, and small-molecule
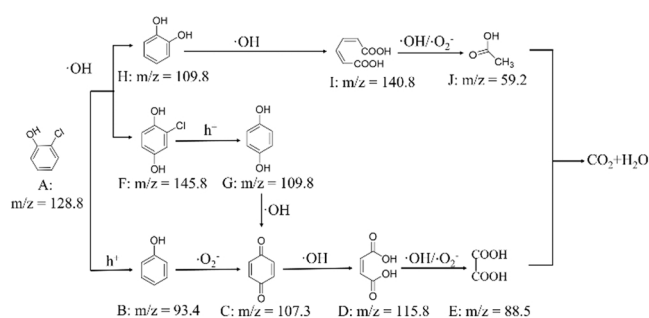

Fig. 9. Proposed degradation path of 2-CP over O-CN/CdS-3.

oxidation processes. Firstly, a single chloride was removed or replaced by -OH under the attack of h$^+$ and·OH to form phenol (B: $m/z = 93.4$), catechol (H: $m/z = 109.8$), and 2-chlorohydroquinone (F: $m/z = 145.8$) further dechlorination into hydroquinone (G: $m/z = 109.8$). Then ·O_2^- and·OH attacked the aromatic ring of phenol (B: $m/z = 93.4$), hydroquinone (G: $m/z = 109.8$) to form p-benzoquinone (C: $m/z = 107.3$), and open ring to form butanediol acid (D: $m/z = 115.8$). On the other hand, catechol (H: $m/z = 109.8$) ruptured under the attack of·OH and produced muconic acid (I: $m/z = 140.8$). Above organic acids reacted with ·O_2^- and·OH radicals were further formed into small molecules like maleic acid (E: $m/z = 88.5$) and formic acid (J: $m/z = 59.2$). Eventually, these small molecules were gradually mineralized into CO_2 and H_2O (Fig. 9). Finally, total organic carbon (TOC) content in the 2-CP solution before and after photocatalysis were detected to uncover the final degradation products of 2-CP (Fig. S18). Since the TOC values decreased from 6.456 mg/L to 1.913 mg/L, the effective TOC removal rate was 71%, indicating that most 2-CP were degraded entirely into CO_2 and H_2O.

4. Conclusion

In summary, a novel Z-type O-CN/CdS heterojunction was successfully prepared through a simple hydrothermal method. The introduction of O adjusted the band structure of g-C_3N_4 to broaden the light response range. The formation of the Z-scheme heterojunction promoted interfacial photogenerated charge separation. Benefiting from the above, the as-synthesized O-CN/CdS photocatalyst could photodegradation 100% of 2-CP within 60 min, and its photocatalytic performance was far superior to the original samples. This perfect photodegradation performance could be owing to (1) porous structure and large specific surface area, (2) OCN/CdS had a relatively narrow bandgap and a wide optical response range, and (3) OCN/CdS formed a novel Z-type heterojunction to promote photogenerated charges separation, improved photocatalytic performance. Furthermore, five catalytic cycles verified that the OCN/CdS photocatalyst exhibits good reusability. Additionally, the effects of different external factors on the photocatalytic degradation ability of OCN/CdS were investigated and it was proved that the photocatalyst holds promise for use in practical applications. This study thus provided guidance for the rational design of efficient Z-scheme photocatalysts for the remediation of refractory CPs in practical applications.

CRediT authorship contribution statement

Zhuzhu Zhang: Data curation, Formal analysis, Methodology, Investigation, Validation, Visualization, Writing – original draft. **Rui Ji:** Investigation. Qimeng Sun: Validation. **Najun Li:** Investigation, Software. **Hua Li:** Data curation, Formal analysis. **Jinghui He:** Writing – review & editing. **Dongyun Chen:** Software, Validation. **Antonio Marcomini:** Data curation, Validation. **Qingfeng Xu:** Conceptualization, Supervision, Writing – review & editing. **Jianmei Lu:** Conceptualization, Supervision, Writing – review & editing.

Declaration of Competing Interest

The authors declare that they have no known competing financial interests or personal relationships that could have appeared to influence the work reported in this paper.

Data Availability

Data will be made available on request.

Acknowledgments

Appendix A. Supporting information

Supplementary data associated with this article can be found in the online version at doi:10.1016/j.apcatb.2022.122276.

References

[1] L. Wang, D.W. Bahnemann, L. Bian, G. Dong, J. Zhao, C. Wang, Two-dimensional layered zinc silicate nanosheets with excellent photocatalytic performance for organic pollutant degradation and CO_2 conversion, Angew. Chem. Int. Ed. 58 (2019) 8103–8108, https://doi.org/10.1002/anie.201903027.

[2] D. Wei, C. Zhao, A. Khan, L. Sun, Y. Ji, Y. Ai, X. Wang, Sorption mechanism and dynamic behavior of graphene oxide as an effective adsorbent for the removal of chlorophenol based environmental-hormones: a DFT and MD simulation study, Chem. Eng. J. 375 (2019), 121964, https://doi.org/10.1016/j.cej.2019.121964.

[3] G. Liu, T. Zhang, T. Wang, H. Yamashita, Y. Zhao, X. Qian, Peroxydisulfate activation by photo-generated charges on mesoporous carbon nitride for removal of chlorophenols, Appl. Catal. B Environ. 296 (2021), 120370, https://doi.org/10.1016/j.apcatb.2021.120370.

[4] K. Li, X. Fang, Z. Fu, Y. Yang, I. Nabi, Y. Feng, A.U. Bacha, L. Zhang, Boosting photocatalytic chlorophenols remediation with addition of sulfite and mechanism investigation by in-situ DRIFTS, J. Hazard. Mater. 398 (2020), 123007, https://doi.org/10.1016/j.jhazmat.2020.123007.

[5] D. Hu, L. Song, R. Yan, Z. Li, Z. Zhang, J. Sun, J. Bian, Y. Qu, L. Jing, Valence-mixed iron phthalocyanines/ (1 0 0) Bi_2MoO_6 nanosheet Z-scheme heterojunction catalysts for efficient visible-light degradation of 2-chlorophenol via preferential dechlorination, Chem. Eng. J. 440 (2022), 135786, https://doi.org/10.1016/j.cej.2022.135786.

[6] J. Liu, D. Han, P. Chen, L. Zhai, Y. Wang, W. Chen, L. Mi, L. Yang, Positive roles of Br in g-C_3N_4/PTCDI-Br heterojunction for photocatalytic degrading chlorophenols, Chem. Eng. J. 418 (2021), 129492, https://doi.org/10.1016/j.cej.2021.129492.

[7] M. Zhang, M. Lu, Z.L. Lang, J. Liu, M. Liu, J.N. Chang, L.Y. Li, L.J. Shang, M. Wang, S.L. Li, Y.Q. Lan, Semiconductor/covalent-organic-framework Z-scheme heterojunctions for artificial photosynthesis, Angew. Chem. Int. Ed. 59 (2020) 6500–6506, https://doi.org/10.1002/anie.202000929.

[8] F.A. Qaraah, S.A. Mahyoub, A. Hezam, A. Qaraah, F. Xin, G. Xiu, Synergistic effect of hierarchical structure and S-scheme heterojunction over O-doped g-C_3N_4/N-doped Nb_2O_5 for highly efficient photocatalytic CO_2 reduction, Appl. Catal. B: Environ. 315 (2022), 121585, https://doi.org/10.1016/j.apcatb.2022.121585.

[9] X. Liu, Y. Du, Y. Zhao, X. Song, X. Jing, L. Yu, M. Sun, 2D Benzodithiophene based conjugated polymer/g-C_3N_4 heterostructures with enhanced photocatalytic activity: Synergistic effect of antibacterial carbazole side chain and main chain copolymerization, Appl. Catal. B: Environ. 312 (2022), 121401, https://doi.org/10.1016/j.apcatb.2022.121401.

[10] Y. Dai, C. Li, Y. Shen, T. Lim, J. Xu, Y. Li, H. Niemantsverdriet, F. Besenbacher, N. Lock, R. Su, Light-tuned selective photosynthesis of azo- and azoxy-aromatics using graphitic C_3N_4, Nat. Commun. 9 (2018) 60, https://doi.org/10.1038/s41467-017-02527-8.

[11] F. Wang, J. Xu, Z. Wang, Y. Lou, C. Pan, Y. Zhu, Unprecedentedly efficient mineralization performance of photocatalysis-self-Fenton system towards organic pollutants over oxygen-doped porous g-C_3N_4 nanosheets, Appl. Catal. B Environ. 312 (2022), 121438, https://doi.org/10.1016/j.apcatb.2022.121438.

[12] S. Balu, Y.-L. Chen, S.-W. Chen, T.C.K. Yang, Rational synthesis of $Bi_xFe_{1-x}VO_4$ heterostructures impregnated sulfur-doped g-C_3N_4: A visible-light-driven type-II heterojunction photo(electro)catalyst for efficient photodegradation of roxarsone

[13] S. Lv, Y.H. Ng, R. Zhu, S. Li, C. Wu, Y. Liu, Y. Zhang, L. Jing, J. Deng, H. Dai, Phosphorus vapor assisted preparation of P-doped ultrathin hollow g-C_3N_4 sphere for efficient solar-to-hydrogen conversion, Appl. Catal. B Environ. 297 (2021), 120438, https://doi.org/10.1016/j.apcatb.2021.120438.

[14] Y. Wang, F. Silveri, M.K. Bayazit, Q. Ruan, Y. Li, J. Xie, C.R.A. Catlow, J. Tang, Bandgap engineering of organic semiconductors for highly efficient photocatalytic water splitting, Adv. Energy Mater. 8 (2018), 1801084, https://doi.org/10.1002/aenm.201801084.

[15] Y. Jiang, Z. Sun, C. Tang, Y. Zhou, L. Zeng, L. Huang, Enhancement of photocatalytic hydrogen evolution activity of porous oxygen doped g-C_3N_4 with nitrogen defects induced by changing electron transition, Appl. Catal. B Environ. 240 (2019) 30–38, https://doi.org/10.1016/j.apcatb.2018.08.059.

[16] Y. Geng, D. Chen, N. Li, Q. Xu, H. Li, J. He, J. Lu, Z-Scheme 2D/2D α-Fe_2O_3/g-C_3N_4 heterojunction for photocatalytic oxidation of nitric oxide, Appl. Catal. B Environ. 280 (2021), 119409, https://doi.org/10.1016/j.apcatb.2020.119409.

[17] W. Li, F. Wang, X.-Y. Liu, Y.-Y. Dang, J.-Y. Li, T.-H. Ma, C.-Y. Wang, Promoting body carriers migration of CdS nanocatalyst by N-doping for improved hydrogen production under simulated sunlight irradiation, Appl. Catal. B Environ. 313 (2022), 121470, https://doi.org/10.1016/j.apcatb.2022.121470.

[18] K. Wang, Z. Xing, D. Meng, S. Zhang, Z. Li, K. Pan, W. Zhou, Hollow $MoSe_2$@Bi_2S_3/CdS core-shell nanostructure as Dual Z-scheme heterojunctions with enhanced full spectrum photocatalytic-photothermal performance, Appl. Catal. B: Environ. 281 (2021), 119482, https://doi.org/10.1016/j.apcatb.2020.119482.

[19] Y. Ren, T. Dong, S. Ding, X. Liu, H. Zheng, L. Gao, J. Hu, AgBr nanoparticles anchored on CdS nanorods as photocatalysts for H_2 evolution, ACS Appl. Nano Mater. 4 (2021) 9274–9282, https://doi.org/10.1021/acsanm.1c01802.

[20] Y. Wang, J. Zhao, W. Hou, Y. Xu, Decoration of CdS nanowires with Ni_3S_4 nanoballs enhancing H_2 and H_2O_2 production under visible light, Appl. Catal. B Environ. 310 (2022), 121350, https://doi.org/10.1016/j.apcatb.2022.121350.

[21] W. Tan, Y. Li, W. Jiang, C. Gao, C. Zhuang, CdS nanospheres decorated with NiS quantum dots as nobel-metal-free photocatalysts for efficient hydrogen evolution, ACS Appl. Nano Mater. 3 (2020) 8048–8054, https://doi.org/10.1021/acsaem.0c01507.

[22] H. Zhao, Z. Xing, S. Su, S. Song, Z. Li, W. Zhou, Gear-shaped mesoporous NH_2-MIL-53(Al)/CdS P-N heterojunctions as efficient visible-light-driven photocatalysts, Appl. Catal. B Environ. 291 (2021), 120106, https://doi.org/10.1016/j.apcatb.2021.120106.

[23] H. Liu, D.-g Cheng, F. Chen, X. Zhan, 2D porous N-deficient g-C_3N_4 nanosheet decorated with CdS nanoparticles for enhanced visible-light-driven photocatalysis, ACS Sustain. Chem. Eng. 8 (2020) 16897–16904, https://doi.org/10.1021/acssuschemeng.0c06004.

[24] R. Zhang, K. Huang, H. Wei, D. Wang, G. Ou, N. Hussain, Z. Huang, C. Zhang, H. Wu, Ultra-low-temperature growth of CdS quantum dots on g-C_3N_4 nanosheets and their photocatalytic performance, Dalton Trans. 47 (2018) 1417–1421, https://doi.org/10.1039/C7DT04355D.

[25] Y. Ran, Y. Cui, Y. Zhang, F. Fang, W. Zhang, X. Yu, H. Lan, X. An, Assembly-synthesis of puff pastry-like g-C_3N_4/CdS heterostructure as S-junctions for efficient photocatalytic water splitting, Chem. Eng. J. 431 (2022), 133348, https://doi.org/10.1016/j.cej.2021.133348.

[26] J. Hu, C. Chen, H. Yang, F. Yang, J. Qu, X. Yang, W. Sun, L. Dai, C.M. Li, Tailoring well-ordered, highly crystalline carbon nitride nanoarrays via molecular engineering for efficient photosynthesis of H_2O_2, Appl. Catal. B Environ. 317 (2022), 121723, https://doi.org/10.1016/j.apcatb.2022.121723.

[27] Y. Zeng, X. Liu, C. Liu, L. Wang, Y. Xia, S. Zhang, S. Luo, Y. Pei, Scalable one-step production of porous oxygen-doped g-C_3N_4 nanorods with effective electron separation for excellent visible-light photocatalytic activity, Appl. Catal. B Environ. 224 (2018) 1–9, https://doi.org/10.1016/j.apcatb.2017.10.042.

[28] J. Zhang, B. Xin, C. Shan, W. Zhang, D.D. Dionysiou, B. Pan, Roles of oxygen-containing functional groups of O-doped g-C_3N_4 in catalytic ozonation: quantitative relationship and first-principles investigation, Appl. Catal. B Environ. 292 (2021), 120155, https://doi.org/10.1016/j.apcatb.2021.120155.

[29] Z. Wang, Z. Wang, X. Zhu, C. Ai, Y. Zeng, W. Shi, X. Zhang, H. Zhang, H. Si, J. Li, C. Z. Wang, S. Lin, Photodepositing CdS on the active cyano groups decorated g-C_3N_4 in Z-scheme manner promotes visible-light-driven hydrogen evolution, Small 17 (2021), 2102699, https://doi.org/10.1002/smll.202102699.

[30] P. Xu, P. Wang, Q. Wang, R. Wei, Y. Li, Y. Xin, T. Zheng, L. Hu, X. Wang, G. Zhang, Facile synthesis of Ag_2O/ZnO/rGO heterojunction with enhanced photocatalytic activity under simulated solar light: kinetics and mechanism, J. Hazard. Mater. 403 (2021), 124011, https://doi.org/10.1016/j.jhazmat.2020.124011.

[31] Z. Yuan, H. Huang, N. Li, D. Chen, Q. Xu, H. Li, J. He, J. Lu, All-solid-state WO_3/$TQDs$/In_2S_3 Z-scheme heterojunctions bridged by Ti_3C_2 quantum dots for efficient removal of hexavalent chromium and bisphenol A, J. Hazard. Mater. 409 (2021), 125027, https://doi.org/10.1016/j.jhazmat.2020.125027.

[32] Z. Zhang, J. Liu, P.-Y. Gu, R. Ji, L. Jin, S. Zhou, J. He, D. Chen, Q. Xu, J. Lu, Preparation of a $Bi_{12}O_{15}Cl_6$@$W_{18}O_{49}$@g-C_3N_4/PDI heterojunction with dual charge transfer paths and its photocatalytic performance for phenolic pollutants, Sep. Purif. Technol. 287 (2022), 120539, https://doi.org/10.1016/j.seppur.2022.120539.

[33] B. Gao, Y. Pan, Q. Chang, Z. Xi, H. Yang, Hierarchically Z-scheme photocatalyst of {0 1 0} $BiVO_4$/Ag/CdS with enhanced performance in synergistic adsorption-photodegradation of fluoroquinolones in water, Chem. Eng. J. 435 (2022), 134834, https://doi.org/10.1016/j.cej.2022.134834.

[34] C. Feng, L. Tang, Y. Deng, J. Wang, J. Luo, Y. Liu, X. Ouyang, H. Yang, J. Yu, J. Wang, Synthesis of leaf-vein-like g-C_3N_4 with tunable band structures and charge

transfer properties for selective photocatalytic H_2O_2 evolution, Adv. Funct. Mater. 30 (2020), 2001922, https://doi.org/10.1002/adfm.202001922.

[35] C.Q. Li, X. Du, S. Jiang, Y. Liu, Z.L. Niu, Z.Y. Liu, S.S. Yi, X.Z. Yue, Constructing direct Z-scheme heterostructure by enwrapping $ZnIn_2S_4$ on CdS hollow cube for efficient photocatalytic H_2 generation, Adv. Sci. (2022), 2201773, https://doi.org/10.1002/advs.202201773.

[36] S. Wang, B. Zhu, M. Liu, L. Zhang, J. Yu, M. Zhou, Direct Z-scheme ZnO/CdS hierarchical photocatalyst for enhanced photocatalytic H_2-production activity, Appl. Catal. B Environ. 243 (2019) 19–26, https://doi.org/10.1016/j.apcatb.2018.10.019.

[37] Y. Zhu, J. Chen, L. Shao, X. Xia, Y. Liu, L. Wang, Oriented facet heterojunctions on CdS nanowires with high photoactivity and photostability for water splitting, Appl.

Catal. B Environ. 268 (2020), 118744, https://doi.org/10.1016/j.apcatb.2020.118744.

[38] P. Sarkar, S. De, S. Neogi, Microwave assisted facile fabrication of dual Z-scheme g-C_3N_4/$ZnFe_2O_4$/Bi_2S_3 photocatalyst for peroxymonosulphate mediated degradation of 2,4,6-Trichlorophenol: the mechanistic insights, Appl. Catal. B Environ. 307 (2022), 121165, https://doi.org/10.1016/j.apcatb.2022.121165.

[39] E. Gómez, R. Cestaro, L. Philippe, A. Serrà, Electrodeposition of nanostructured Bi_2MoO_6@Bi_2MoO_{6-x} homojunction films for the enhanced visible-light-driven photocatalytic degradation of antibiotics, Appl. Catal. B Environ. 317 (2022), 121703, https://doi.org/10.1016/j.apcatb.2022.121703.